**ORIGINAL PAPER**

# Early release of H$_2$O during subduction of carbonated ultramafic lithologies

Lisa Eberhard[1,2] · Oliver Plümper[2] · Daniel J. Frost[1]

## Abstract

To investigate the effect of carbon-bearing phases on the release of fluids in subducted serpentinites, we performed high-pressure multi-anvil experiments on representative ophicarbonate assemblages over a pressure range from 2.5 GPa to 5 GPa and from 450 °C to 900 °C, across the antigorite-out reaction. Parallel experiments were performed on carbonate-free serpentinites. In all experiments, we monitored and/or controlled the oxygen fugacity. The addition of 20 wt. % CaCO$_3$ to a serpentinite assemblage at 2.5 GPa is found to decrease the onset of the serpentine dehydration by over 100 °C, in comparison to carbonate-free assemblages. Similarly, the final disappearance of serpentine is also affected by the presence of CaCO$_3$. For a bulk CaCO$_3$ content of 20 wt. %, this causes a decrease in maximum stability of antigorite by 50 °C. For a bulk CaCO$_3$ content exceeding 25 wt. %, this difference can be as high as 100 °C in warm and 150 °C in cold subduction zones, causing antigorite to be completely dehydrated at 500 °C. This results from the reaction of CaCO$_3$ with serpentine to form clinopyroxene and Mg-rich carbonates. This reaction, however, causes no discernible decrease in the proportion of carbonate, indicating that the amount of released carbon is insignificant. Whilst CaCO$_3$, therefore, influences serpentine stability, there is no significant effect of hydrous phases on the carbonate stability. On the other hand, a MgCO$_3$-bearing system shows no significant effects on the serpentinite stability field. Further experiments and oxygen fugacity calculations indicate that graphite is not stable in typical magnetite-bearing serpentinites. The reduction of carbonates to graphite would require oxygen fugacities that are 1–2 log units below those of magnetite-bearing serpentinites. This confirms earlier studies and indicates that reduction of carbonates can only occur through the infiltration of external H$_2$-rich fluids.

**Keywords** Ophicarbonates · Subduction zones · Dehydration reaction · Decarbonation reaction · High PT-experiment

## Introduction

The subduction of volatile-bearing slabs into the Earth's interior is an important part of the deep volatile cycle. Whilst significant discrepancies exist on the fraction of volatiles that are subducted and released through devolatilisation (Kerrick and Connolly 1998; van Keken et al. 2011; Dasgupta 2013; Kelemen and Manning 2015), it is widely

accepted that their release drives numerous processes in the upper mantle, such as mantle metasomatism and partial melting related to arc volcanism (Guillot et al. 2000; Pirard and Hermann 2015; Scambelluri et al. 2016). To better understand how these volatiles are transported between different reservoirs, it is crucial to determine the forms in which they are stable at different conditions and how they interact with co-existing phases.

Hydrogen is mainly transported in hydrous minerals in the oceanic lithosphere, which form from fluid–rock interactions at the ocean floor. The serpentinised lithospheric mantle likely plays a crucial role in the hydrogen cycle and is estimated to contain up to half of the total subducted hydrogen (Rüpke et al. 2004; van Keken et al. 2011). Carbon is mainly subducted as carbonate minerals and organic carbon residues (Plank and Manning 2019). The ratio between the oxidised and reduced carbon varies between different lithological layers and between different slabs. In the sediment

✉ Lisa Eberhard
  l.eberhard@uu.nl

1  Bayerisches Geoinstitut, University of Bayreuth, Universitätsstrasse 30, 95440 Bayreuth, Germany

2  Department of Earth Sciences, Utrecht University, Vening Meineszgebouw A, Princetonlaan 8a, 3584 CB Utrecht, Netherlands

layer, organic and inorganic remains of organisms make a significant fraction of the bulk carbon. In the serpentinised lithospheric mantle, carbonates are formed through direct precipitation from the circulating ocean water and through a sequence of carbonation reactions, forming ophicarbonates, soapstones and listvenites (Driesner 1993; Kelemen et al. 2011; Schwarzenbach et al. 2013; Clerc et al. 2014). However, minor amounts of graphite can also form in this lithology through the reduction of carbonates if the $f(O_2)$ is sufficiently low (Kelemen et al. 2011; Vitale Brovarone et al. 2017).

At the elevated pressures and temperatures ($PT$) of subduction zones, mineral-bound water is released in a series of dehydration reactions. Besides the well-documented brucite-, antigorite- and chlorite-out reactions (Ulmer and Trommsdorff 1995; Padrón-Navarta et al. 2010; Plümper et al. 2016; Piccoli et al. 2019; Ferrand 2019), these also include less well-constrained reactions, such as the phase transition from lizardite to antigorite (Schwartz et al. 2013) and prograde decrease in the polysome length of antigorite (Wunder et al. 2001). Most of these reactions are not univariant and occur over a certain temperature interval. The onset is typically marked by the first appearance of anhydrous reaction products, e.g. olivine-in, whereas the upper temperature boundary is the final disappearance of the hydrous reactant. Often, several generations of reaction products can be found in a single specimen but can be distinguished based on their chemical composition and microstructures, and can be assigned to specific dehydration reactions (Jabaloy-Sánchez et al. 2022).

The release of hydrous fluids during prograde subduction has the potential to transport solute species from the slab into the mantle wedge (Frezzotti et al. 2011; Ague and Nicolescu 2014; Piccoli et al. 2016; Tian et al. 2019; Kelemen et al. 2022), which ultimately links the deep cycle of both hydrogen and carbon. Disordered organic carbon is continuously leached by these fluids through oxidative dissolution at shallow levels in the subduction zone, whilst highly ordered graphitic material seems to be more stable but dissolves more readily at subarc depth of $> 110$ km (Plank and Manning 2019; Tumiati et al. 2020, 2022). The release of carbon from subducting slabs also occurs through dissolution of carbonate minerals in aqueous fluids (Facq et al. 2014; Farsang et al. 2021). At least in low-pressure environments ($< 2$ GPa), there is evidence that $CO_2$ can be released through decarbonation reactions, in the presence of aqueous fluids (Kerrick and Connolly 1998; Eberhard and Pettke 2021). Other studies suggest that more reduced carbon can be dissolved in the fluid (Sverjensky et al. 2014; Vitale Brovarone et al. 2020).

We hypothesise that not only hydrous minerals affect the stability of carbon-bearing phases but that also the presence of the latter influences the release of aqueous fluids.

To examine the mutual influences hydrogen and carbon may have on volatile-bearing phase stability in subducting slabs, we performed multi-anvil experiments on carbonated serpentinites. The mineralogy in the run products was analysed with respect to pressure, temperature and the oxygen fugacity $f(O_2)$. We, thus, provide the first detailed experimental investigation on ophicarbonates at elevated pressure and temperature. Our experiments were performed on the system serpentine $+ CaCO_3$ and we extend our findings to serpentine $+ MgCO_3$ through thermodynamic modelling. The results constrain the effects of carbonates on the stability of serpentine, as well as the amount of fluid produced and carbon recycled. Additional experiments were performed on a mixture of serpentine $+$ graphite $\pm CaCO_3$. These experiments determine the effect of $f(O_2)$ and can be used as a proxy to investigate subducted lithologies containing both oxidised and reduced carbon.

## Methods

### Starting material

We performed multi-anvil experiments on synthetic ophicarbonate samples using mixtures of natural antigorite (Zer_1701) and natural lizardite (Lig_1602) powders mixed with $CaCO_3$. Carbonate-free experiments were also performed at similar conditions on both serpentinite samples. The antigorite-serpentinite is from a boulder collected in Zermatt, Switzerland, containing $> 95\%$ antigorite, $< 5\%$ magnetite and minor sulphides. The sample is comparable to the serpentine mylonite described in Li et al. (2004) and does not contain chlorite, olivine or diopside. The lizardite-serpentinite is a massive serpentinite from Val Graveglia, Italy, consisting of $> 90\%$ lizardite with $< 5\%$ opaque phases (not further distinguished) and minor chlorite. The two samples were chosen based on their high serpentine content of $> 90\%$ and different serpentine polysomes. We note that they differ in their mineralogy, bulk Al and FeO content (compare supplementary material), which can have small effects on the stability of individual serpentine phases. However, the interaction between the silicate and carbonate fractions in subducted serpentinites, will not be significantly affected by these chemical and mineralogical differences.

The serpentine powders were prepared using an agate pestle mill. The resulting grain size was in the range of 20 μm to 50 μm. For most experiments, the serpentine powder was mixed with 5 wt. % Ir metal powder, serving as a sliding redox sensor (Stagno and Frost 2010). To obtain carbonated serpentinite starting materials, the antigorite powder was mixed with 20 wt. % Ca-carbonate and the lizardite powder with 10 wt. % Ca-carbonate, respectively. Additional antigorite and lizardite starting materials

were also produced where the $f(O_2)$ was buffered by the presence of both Ca-carbonate (8 wt. %) and graphite (2 wt. %). In one experiment (V1143b), 10 wt. % graphite was added to a lizardite sample without carbonate. All starting materials are summarised in Table 1.

**Table 1** Summary of experiments conducted in this study

| Sample name | P [GPa] | T [°C] | Time [h] | Starting material | Run products |
|---|---|---|---|---|---|
| *Antigorite* | | | | | |
| V1090 | 4 | 570* | 62 | 5 wt. % Ir | Atg, Mgt, (ps) |
| V1104 | 3 | 580* | 86 | 5 wt. % Ir | Atg, Mgt, (ps) |
| V1105 | 3 | 630* | 86 | 5 wt. % Ir | Atg, Chl, Ol, (Opx)[+], Mgt |
| V1111 | 3 | 670 | 62 | 5 wt. % Ir | Atg, Chl, Ol, (Opx)[++] |
| *Carbonated antigorite* | | | | | |
| V1079 | 3 | 450 | 112 | 4 wt. % Ir + 20 wt. % Cal | Atg, Arag, Mgt, (ps) |
| V1124 | 3 | 550 | 99 | 4 wt. % Ir + 20 wt. % Cal | Atg, Arag, Mgt, (ps) |
| V1234a | 3 | 550 | 72 | 4 wt. % Ir + 20 wt. % Cal | Atg, (Cpx)[++], Arag, Mgt |
| V1082 | 2.5 | 560* | 87 | 4 wt. % Ir + 20 wt. % Cal | Atg, Chl, Ol, (Cpx)[++], Dol, (Spl) |
| V1076 | 2.5 | 650 | 86 | 4 wt. % Ir + 20 wt. % Cal | Chl, Ol, (Cpx)[++], Dol, Ca-rich carbonate, (Mgt), Spl |
| V1071 | 2.5 | 700 | 72 | 4 wt. % Ir + 20 wt. % Cal | Chl, Ol, (Cpx)[++], Dol, Mgs, Mgt |
| V1060 | 2.5 | 750* | 65 | 20 wt. % Cal | Chl, Ol, (Cpx)[++], Dol, Mgt |
| V1062 | 2.5 | 780* | 92 | 4 wt. % Ir + 20 wt. % Cal | Ol, Cpx, Dol, Spl |
| V1064 | 2.5 | 800* | 76 | 4 wt. % Ir + 20 wt. % Cal | Ol, Cpx, Grt, Dol, Spl |
| V1077 | 2.5 | 800* | 67 | 4 wt. % Ir + 20 wt. % Cal | Ol, Cpx, Grt, Dol |
| V1103 | 3 | 800 | 91 | 4 wt. % Ir + 20 wt. % Cal | Ol, Cpx, Grt, Dol, Mgs, Spl |
| V1065 | 2.5 | 820* | 73 | 4 wt. % Ir + 20 wt. % Cal | Ol, Cpx, Grt, Dol, Spl |
| V1099 | 3 | 880* | 68 | 4 wt. % Ir + 20 wt. % Cal | Ol, Cpx, Grt, Dol, Mgs |
| V1089 | 4 | 900* | 86 | 4 wt. % Ir + 20 wt. % Cal | Ol, Cpx, (Grt)[++], Dol, Mgs |
| V1050 | 2.5 | 900* | 46 | 4 wt. % Ir + 20 wt. % Cal | Ol, Cpx[++], Grt, Cal, Dol |
| *Antigorite buffered* | | | | | |
| V1148a | 3 | 500 | 97 | 8 wt. % Cal, 2 wt. % Gr | Atg, Cpx, Arag, Mgt, Gr |
| V1153b | 5 | 500 | 98 | 8 wt. % Cal, 2 wt. % Gr | Atg, Cpx, (Ol)[++], Mgs, Mgt, Gr |
| *Lizardite* | | | | | |
| V1125 | 3 | 500 | 80 | 5 wt. % Ir | Liz, (ps), Mgt |
| V1114 | 3 | 550 | 98 | 5 wt. % Ir | Liz, Chl, Ol, (Opx)[++], (Mgt) |
| V1116 | 3 | 600 | 192 | 5 wt. % Ir | Liz, Chl, Ol, (Opx)[++], Mgt |
| *Carbonated lizardite* | | | | | |
| V1234b | 3 | 550 | 72 | 4 wt. % Ir + 20 wt. % Cal | Liz, Cpx, (Ol)[++], Mgs, (Mgt) |
| V1233a | 3 | 600* | 72 | 4 wt. % Ir + 20 wt. % Cal | Chl, Ol, Cpx, Mgs, (Mgt) |
| V1232a | 3 | 800* | 73 | 4 wt. % Ir + 20 wt. % Cal | Ol, Cpx, Grt, Dol, Spl |
| *Lizardite buffered* | | | | | |
| V1143b | 3 | 500 | 90 | 10 wt. % Gr | Liz, Ol, (Mgt), Gr |
| V1148b | 3 | 500 | 97 | 8 wt. % Cal + 2 wt. % Gr | Liz, (Cpx)[++], (Ol)[++], Mgs, Mgt, Gr |
| V1153a | 5 | 500 | 98 | 8 wt. % Cal + 2 wt. % Gr | Liz, (Cpx)[++], (Ol)[++], Mgs, (Mgt), Gr |

Starting material indicates the mass fraction of Ir metal, carbonate and/or graphite added to the serpentine powder. Abbreviations are as follows: *Ir* iridium metal, *ps* secondary phases (not further distinguished), *Atg* antigorite, *Liz* lizardite, *Mgt* magnetite, *Ol* olivine, *Chl* chlorite, *Opx* orthopyroxene, *Cpx* clinopyroxene, *Cal* calcite, *Arag* aragonite, *Dol* dolomite, *Mgs* magnesite, *Gr* graphite, *Spl* spinel, *Grt* garnet. Minerals in brackets were identified with EDX but were too fine grained for quantitative chemical analyses. Minerals marked with [+] were extrapolated from analysis trends. The composition of minerals marked with [++] was estimated from other experiments (see supplementary material for more details). In experiments marked with *, the temperature was estimated based on temperature–power relations due to thermocouple failure

## High-pressure experiments

We run the experiments in 18 mm edge length octahedra, with tungsten carbide cubes that have 11 mm edge length truncated corners (Keppler and Frost 2005). The capsules were prepared from gold tubes and welded at both ends to prevent fluid loss during the experiment. High temperatures were generated using a stepped graphite heater and controlled with a type-D thermocouple. In case of thermocouple failure, the temperature was estimated from power–temperature relations and run product mineral assemblages. We used a 500 tonne multi-anvil press at the Bayerisches Geoinstitut (BGI) equipped with a Walker module. *PT* conditions were chosen across the antigorite and chlorite dehydration reaction (450 °C to 900 °C) for a range of typical subduction pressures of 2.5 to 5 GPa (Syracuse et al. 2010). Conditions of all experiments are provided in Table 1.
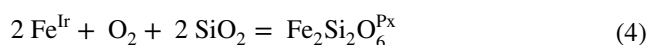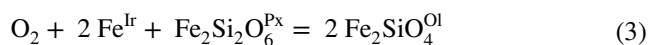
## Analytical methods

The run products were first examined with a GEMINI LEO 1530 electron microscope run at 20 kV acceleration voltage. Minerals were identified using energy-dispersive X-ray (EDX) analysis. Detailed compositions of the identified mineral phases were measured with a JEOL 8200 electron microprobe (EMP) operating at an acceleration voltage of 15 kV. The beam current and diameter were optimised for each phase: 20 nA with a focussed beam was used for garnet, olivine, pyroxene, oxides and alloys; and 10–15 nA and a 2–5 μm beam spot was used for serpentine, chlorite and carbonates. Calibration was performed in each session on silicates, oxides and metals. A San Carlos olivine was measured as a secondary standard to check consistency between the sessions. The composition of mineral phases and standard deviations in each run product are given in the supplementary material. If only one grain of a phase could be measured, we report a 2% error.

Ca-carbonate polymorphs and serpentine polysomes in the experimental products were identified by Raman spectroscopy, using a WiTec ALPHA300 R confocal microscope, equipped with a 532 nm laser, 50× objective lens and a spectral grating of 1800 grooves/cm. Data acquisition and processing was performed with WiTec ProjectFive software.

Mass balance calculations were performed using the major element compositions of each phase in the run product and the starting material. The fluid in the run products was assumed to be pure $H_2O$ and estimated from oxide differences. This assumption is justified by the generally low solubility of carbonate minerals in aqueous fluids at the experimental *PT* conditions (Facq et al. 2014; Menzel et al. 2020; Farsang et al. 2021). In some experiments, pyroxenes and olivines were too fine grained to be accurately measured with EMP (compare Fig. 2b, c, e, f). In

this case, the composition of the phases was either estimated from analyses trends or estimated from other experiments performed at similar conditions. We used a Monte Carlo approach to account for uncertainties from the analyses of the product minerals and the starting compositions. One thousand individual minimisations were performed for each experiment. The starting material and run product composition were randomly sampled around their normal distribution for each minimisation. Reported in the supplementary material are mean values and standard deviations.

The experimental $f(O_2)$ was determined using various equilibria involving oxides, silicates and the Ir sliding redox sensor:

$$3\,Fe^{Ir} + 2\,O_2 = Fe_3O_4^{Mgt} \tag{1}$$

$$O_2 + 2\,Fe^{Ir} + SiO_2 = Fe_2SiO_4^{Ol} \tag{2}$$

$$O_2 + 2\,Fe^{Ir} + Fe_2Si_2O_6^{Px} = 2\,Fe_2SiO_4^{Ol} \tag{3}$$

$$2\,Fe^{Ir} + O_2 + 2\,SiO_2 = Fe_2Si_2O_6^{Px} \tag{4}$$

$$2\,Fe_3O_4^{Mgt} + 3\,SiO_2 = 3\,Fe_2SiO_4^{Ol} + O_2 \tag{5}$$

$$2\,Fe_3O_4^{Mgt} + 6\,SiO_2 = 3\,Fe_2Si_2O_6^{Px} + O_2 \tag{6}$$
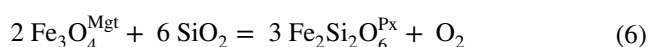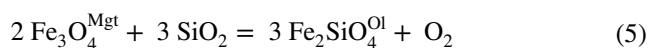
As there is no pure $SiO_2$ phase stable in our experiments, the chemical potential of the $SiO_2$ component is calculated from olivine and pyroxene through the equilibrium

$$Mg_2SiO_4^{Ol} + SiO_2 = Mg_2Si_2O_6^{Px}. \tag{7}$$
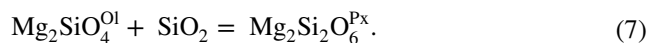
Oxygen fugacities were calculated using thermodynamic data from Holland and Powell (2011). The activity-composition relation of the Ir redox sensor was taken from Stagno and Frost (2010). For olivine, orthopyroxene and clinopyroxene, a symmetrical mixing model was used with macroscopic interaction parameters of 9 kJ/mol, 5.2 kJ/mol and 20 kJ/mol, respectively (Evans and Powell 2015; Jennings and Holland 2015). Where possible, we used several equilibria to test for internal consistency with the mean values reported in the supplementary material. For experiments buffered with carbonate + graphite, the $f(O_2)$ was determined using equilibria (9) and (10), discussed latter.

Phase diagrams were calculated with Perple_X version 6.9.0 (Connolly 1995). We used the HP11 database together with the fluid equation of state of Pitzer and Sterner (1995). We calculated *PT* pseudosections for pure and carbonated serpentinites. The bulk composition used was derived from the antigorite-serpentinite used in this study (97 wt. % antigorite + 3 wt. % magnetite) as: $SiO_2 = 39.5$ wt. %, $MgO = 36.5$

wt. %, $Al_2O_3 = 2.4$ wt. %, $FeO = 6.9$ wt. %, $H_2O = 13.75$ wt. %. Either 20 wt. % $CaCO_3$ or $MgCO_3$ were used to calculate carbonated systems. To derive the dehydration surface in the 3D space, an additional 41 isobaric *T-X* pseudosections were calculated in the range from 1 to 5 GPa for *X* ranging from pure antigorite-serpentinite to antigorite-serpentinite + 50 wt. % $CaCO_3$. All calculations were buffered at the fayalite–magnetite–quartz equilibrium (FMQ), based on our results that show the experimental $f(O_2)$ to be close to the FMQ buffer (compare Fig. 4). The Al content in pyroxene in our experiments is below 3 wt. % (except for 4.4 wt. % in experiment V1050 conducted at lower pressure). Based on this observation, we excluded Tschermak-pyroxene endmembers. For simplicity amphibole Al endmembers were also excluded as Eberhard and Pettke (2021) measured low-Al contents in tremolite within dehydrated ophicarbonates. Included solid solution models were O(JH), Grt(JH), Opx(JH), Cpx(JH), Sp(JH), Chl(HP), Atg(PN), oCcM(EF), GlTrTsPg, o-Amph, B, T and A phase (here the terms in brackets refer to models from JH: Jennings and Holland (2015); HP: Holland et al. (1998); PN: Padrón-Navarta et al. (2013), EF: Franzolin et al. (2011). GlTrTsPg is a non-ideal model with interaction parameters from Wei and Powell (2003) and White et al. (2003). All other solid solution models assume ideal mixing). The choice of Chl(HP) over Chl(W) was made as initial tests led to unrealistically high chlorite contents at low temperatures. Also note that in the current set of solution models, $Fe^{3+}$ content in antigorite is not computed. The fluid was modelled as a $H_2O$–$CO_2$ binary (Connolly and Trommsdorff 1991).

# Results

Table 1 gives an overview of the phases found in each experiment. Mineral compositions of each phase, as well as the mass balance-determined phase modes can be found in the supplementary material. Below, experimental results are presented followed by thermodynamic calculations. Unbuffered and buffered oxygen fugacity experiments on antigorite-bearing and lizardite-bearing experiments are presented in turn.

The serpentine polysomes in the experimental products were analysed by Raman spectroscopy. Antigorite remained stable in pure and carbonated experiments up to a temperature of 570 °C (Table 1; Fig. 1a). Similarly, also lizardite-bearing experiments do show serpentine at temperature ≤ 600 °C (Fig. 1b). We also analysed the
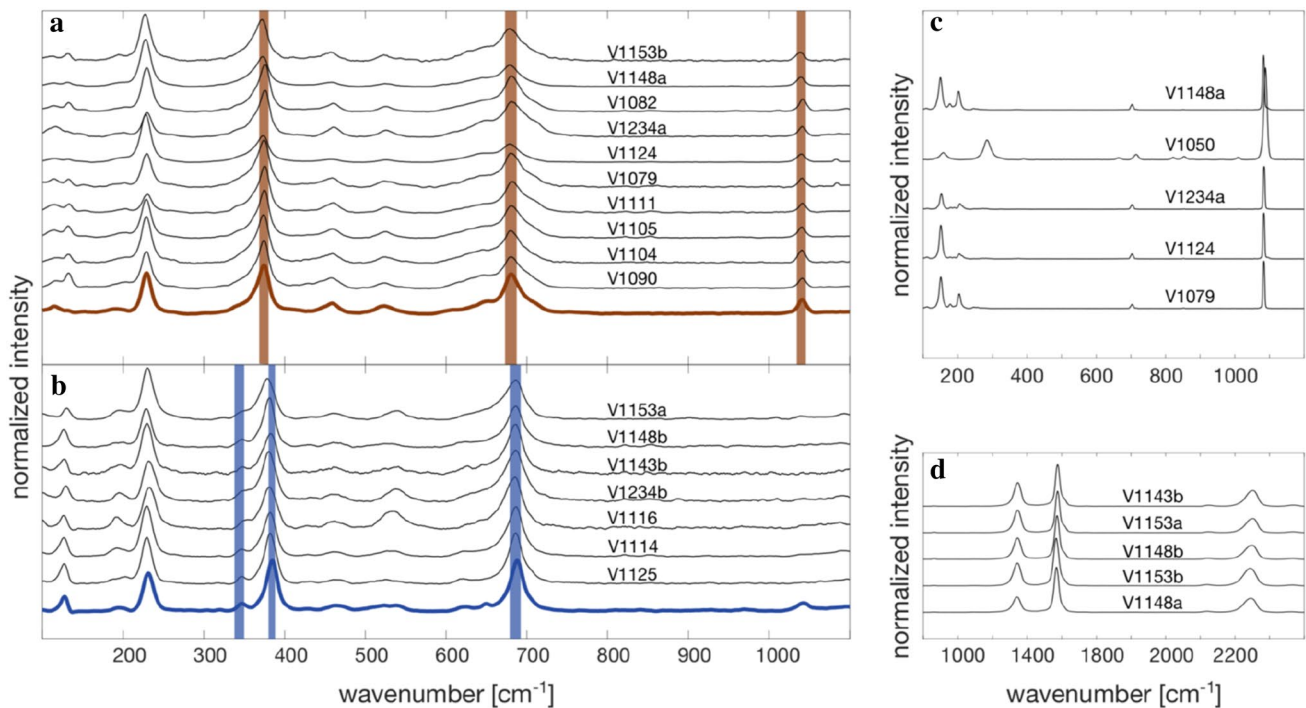


**Fig. 1** Raman spectra of serpentine and carbon-bearing phases. **a** antigorite starting material (coloured) and experimental products (black) do show similar major peaks highlighted in brown. **b** Lizardite starting material (coloured) and experimental products (black) do show similar major peaks, which are slightly shifted with respect to antigorite. Note the slightly higher wavenumber for the major peaks and an additional minor peak at 355 $cm^{-1}$. **c** Ca-carbonates in the run products are mainly aragonite. Calcite is only observed at high temperature and low pressure, e.g. in experiment V1050 (900 °C, 2.5 GPa). **d** Graphite in experimental products indicating an intermediate state of ordering
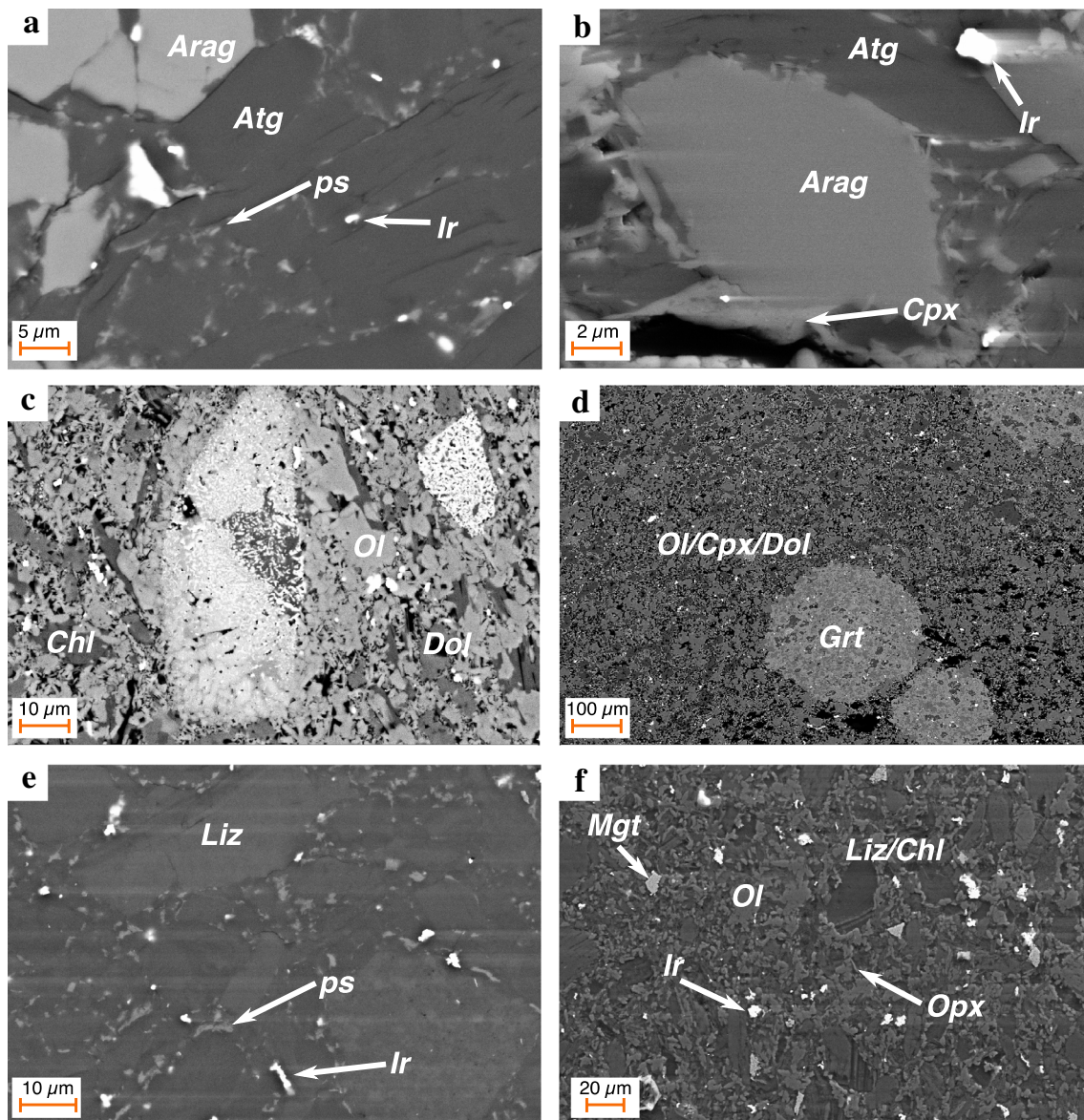
**Fig. 2** Mineral assemblages in run products: **a** V1079 run at 450 °C and 3 GPa. The sample contains angular carbonate grains embedded in an antigorite matrix. Disseminated Ir alloys can also be observed. Submicrometric secondary phases (ps) along antigorite grain boundaries formed from dehydration reaction. **b** V1234a run at 550 °C and 3 GPa. Very early Fe-rich silicates can be found around the carbonate grains. **c** V1076 run at 650 °C and 2.5 GPa. With increasing temperature, magnetite disappears leaving only its outline marked by fine-grained Cr-rich spinel. **d** V1065 run at 900 °C and 2.5 GPa. At temperatures exceeding the final dehydration reaction, garnets can be observed. Garnets usually form roundish grains with abundant inclusions. **e** V1125 run at 500 °C and 3 GPa. Submicrometric secondary phases (ps) form along lizardite grain boundaries. **f** V1116 run at 600 °C and 3 GPa. Olivine and orthopyroxene from a dense network between lizardite and chlorite grains

different Ca-rich carbonates (Fig. 1c). Experiments at pressures $\geq 3$ GPa contain aragonite. Only, at 2.5 GPa (V1050), was calcite observed. Unfortunately, it was not possible to analyse the Ca-rich carbonate in V1076 as this sample was lost during preparation for additional analyses. Raman spectra of graphite in experimental products are shown in Fig. 1d and indicate a high degree of ordering based on the high intensity of the band at 1570 cm$^{-1}$.

The carbonate-free antigorite-bearing experiments contain a minor amount of secondary phases along antigorite grain boundaries at temperatures $\leq 580$ °C. These phase dehydration reaction products, however, were too small to be identified by EDX and/or Raman spectroscopy. With increasing temperature from 580 °C to 670 °C, chlorite starts to coexist with antigorite, and olivine and orthopyroxene could be identified, although the grain size and needle-like
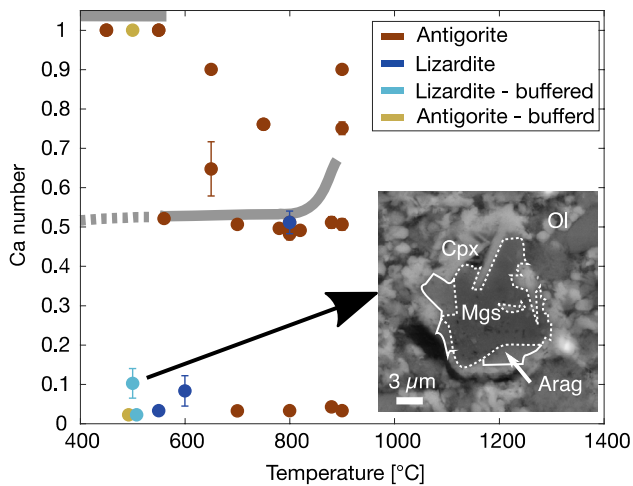
**Fig. 3** Composition of carbonates in unbuffered experiments as a function of temperature. The Ca number, being molar CaO/ (CaO+FeO+MgO), decreases stepwise to dolomite and magnesite in antigorite-bearing experiments with increasing temperature. The grey lines mark results from thermodynamic calculation, i.e. carbonate composition along isobaric path indicated in Fig. 5e (white line). The solid line indicates major carbonate phase (> 15 wt. %) and the dashed the minor carbonate phase (< 2 wt. %). The buffered antigorite-bearing experiments do show magnesite already at low temperatures. Some experiments show magnesite or dolomite with elevated Ca content. The inset shows experiment V1148b, having such aragonite intergrowth with magnesite. Dashed and solid white lines indicate the outline of magnesite and aragonite, respectively
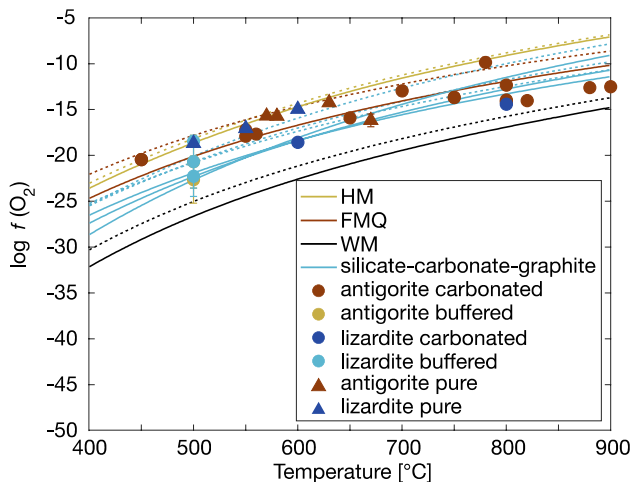


**Fig. 4** Calculated f(O₂) of run products. All experiments have an f(O₂) close to the FMQ buffer. Lines show various f(O₂) buffers at 3 GPa (solid) and 5 GPa (dotted). Buffers are calculated with HP11 database (Holland and Powell 2011) and Pitzer and Sterner fluid EoS (Pitzer and Sterner 1995), assuming composition of all phases. Abbreviations are as follows: HM hematite–magnetite buffer, FMQ fayalite–magnetite–quartz buffer, WM wustite–magnetite buffer. Silicate–carbonate–graphite buffer refers to reaction (8), (9) and (10)

texture of the later did not allow for EPM measurements. Antigorite disappears from the assemblage above 670 °C in agreement with previous studies (Bromiley and Pawley 2003; Padrón-Navarta et al. 2010). Also observed is the disappearance of the magnetite with increasing temperature. Similarly, also the carbonated antigorite-bearing experiments contain submicrometric grains along serpentine grain boundaries (Fig. 2a) at low temperatures (V1079 and V1124, run at 3 GPa and 450 °C and 550 °C, respectively). The carbonate content, obtained from mass balance calculations, is 19.8(5) wt. % and is equal to the starting material carbonate content. Experiment V1234a, run also at 3 GPa and 550 °C indicates the formation of submicrometric needle-like secondary phases (Fig. 2b), growing preferentially along the carbonate–silicate interface and along antigorite grain boundaries. Based on EDX analyses, these phases were identified as clinopyroxene, although their small grain size did not allow for quantitative EMP analyses. Increasing temperature results in an increase in the abundance of clinopyroxene and the formation of 6(2) wt. % chlorite at 560 °C (V1082), with the mode of antigorite decreasing to 21(7) wt. %. At these conditions, the stable carbonate is dolomite, although the total carbonate fraction remains at 19.4(8) wt. %. At temperatures between 650 °C and 750 °C (V1076, V1071, V1060), antigorite has fully broken down and chlorite becomes the only water-bearing phase (7(2)–9(2) wt. %), with dolomite remaining as the major carbonate phase. The total carbonate fraction makes up 17(1)–20(3) wt. %, representing only a minor decrease in the carbonate content with increasing temperature. In experiment V1071 (2.5 GPa, 700 °C), a small amount (approx. 3 wt. %) of magnesite is observed, in addition to dolomite. With increasing temperature, magnetite is gradually replaced by Cr-rich spinel, which outlines the relicts of former magnetite grains in some samples (Fig. 2c). The last dehydration reaction, i.e. chlorite-out, occurs between 750 °C and 780 °C. Experiments performed at temperatures above this reaction contain olivine, clinopyroxene and garnet ± Cr-rich spinel (Fig. 2d). At these temperatures, dolomite is the only stable carbonate at 2.5 GPa. At higher pressures (3–4 GPa), dolomite is joined by minor magnesite. The total carbonate fraction is ∼ 18 wt. %. Minor calcite persisted in experiment V1050 (2.5 GPa, 900 °C) potentially due to the relatively short run duration, as a longer experiment at the same conditions (V1065) produced only dolomite.

The carbonate compositions are close to end-member aragonite, dolomite and magnesite. Only a few experiments, all performed at 2.5 GPa, have a higher Mg content in the Ca-rich carbonate (V1076, V1062, V1050). In V1050, the presence of calcite was confirmed (Fig. 1c). It is, thus, possible that the deviation from pure Ca-endmember is due to a higher solubility of Mg in Ca-carbonate with respect to aragonite, which is stable in experiments performed > 3 GPa (Hermann et al.
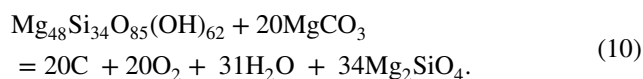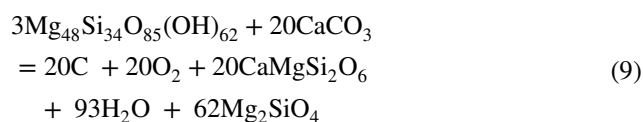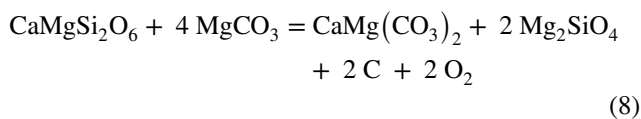
2016). Another possibility would be that fine-grained intergrowth of calcite and dolomite caused an intermediate composition. Such intergrowth is observed in experiment V1148b, causing a higher Ca content in magnesite with respect to the thermodynamic calculations (Fig. 3).

Two antigorite-bearing experiments were performed at 500 °C, with the $f(O_2)$ buffered by the presence of graphite and carbonate in the assemblage. In both experiments, the formation of clinopyroxene can be observed. At 3 GPa (V1148a), aragonite is stable together with minor clinopyroxene (< 1 wt. %). At 5 GPa (V1153b), however, 17(1) wt. % clinopyroxene formed and the co-existing carbonate is magnesite, with mass balance indicating that the carbonate fraction increased from 7 wt. % to 11 wt. %. The proportion of antigorite decreased from approximately 88 wt. % to 51 wt. %.

Similar phase relations were observed in the lizardite-bearing experiments, though at slightly lower temperatures. The carbonate-free lizardite-bearing experiments likewise show the formation of submicrometric secondary phases at 500 °C (Fig. 2e). The formation of chlorite is observed at temperatures as low as 550 °C. This first dehydration reaction goes along with the formation of olivine and orthopyroxene (Fig. 2f). Whilst 18 wt. % lizardite persisted in the carbonate-free experiment at 600 °C (V1116), lizardite is fully dehydrated at the same conditions in the carbonated system (V1233a), along with the formation of 20 wt. % clinopyroxene. The stable carbonate in the lizardite-bearing experiments is magnesite at low temperature and dolomite in the fully dehydrated sample (V1232a).

The lizardite-bearing experiment V1153a, with an $f(O_2)$ buffered by carbonate and graphite, reveals the same phase relations as the respective antigorite-bearing experiment (V1153b). At lower pressures, i.e. 3 GPa, experiment V1148b shows the presence of magnesite and significantly more clinopyroxene with respect to V1148a. In experiment V1143b, only graphite was added to the lizardite starting material. No carbonate was formed but lizardite broke down to form an assemblage containing a significant proportion of olivine (32 wt. %) with a relatively low Mg#, i.e. Mg/(Mg + Fe), of 0.83. Magnetite is still observed in this experiment but reveals an extremely porous texture.

The calculated $f(O_2)$ of all experiments is shown in Fig. 4 and is very close to the FMQ oxygen buffer (supplementary material). Three curves are shown for equilibria within slightly different assemblages containing both carbonate and graphite:

$$CaMgSi_2O_6 + 4\,MgCO_3 = CaMg(CO_3)_2 + 2\,Mg_2SiO_4 + 2\,C + 2\,O_2 \tag{8}$$

$$3Mg_{48}Si_{34}O_{85}(OH)_{62} + 20CaCO_3$$
$$= 20C + 20O_2 + 20CaMgSi_2O_6 \tag{9}$$
$$+ 93H_2O + 62Mg_2SiO_4$$

$$Mg_{48}Si_{34}O_{85}(OH)_{62} + 20MgCO_3$$
$$= 20C + 20O_2 + 31H_2O + 34Mg_2SiO_4. \tag{10}$$

These equilibrium curves are all within approximately 1 log unit of each other at conditions where antigorite is stable except at temperatures ≤ 500 °C. The $f(O_2)$ in experiments where carbonate coexists with graphite is calculated using the equilibrium applicable to the particular assemblage.

Figure 5a–c shows calculated pseudosections for a pure antigorite-serpentinite and the same serpentinite with an additional 20 wt. % $CaCO_3$ and 20 wt. % $MgCO_3$, respectively. The general topology is similar in all pseudosections to the extent that antigorite dehydrates to chlorite, which further dehydrates to spinel/garnet. However, the dehydration starts at significantly lower temperature in the $CaCO_3$-bearing system. Figure 5d–f shows the fraction of released $H_2O$. In the pure antigorite-serpentinite, Fig. 5d, the fluid is stepwise released through dehydration reactions, which are mainly temperature dependent at the pressure range of interest. At 2.5 GPa (white line in Fig. 5d), these are the antigorite-out at 600 °C–650 °C and the chlorite-out at 800 °C. In the system with $CaCO_3$, the antigorite-out reaction occurs over the temperature range 430 °C to 580 °C at 2.5 GPa. Moreover, the antigorite-out reaction is also strongly pressure dependent: At pressures exceeding 4 GPa, a significant amount of fluid is released at temperatures < 550 °C. The $MgCO_3$-bearing system, however, shows a similar dehydration temperature for antigorite and chlorite at low to intermediate pressures (< 3 GPa) with respect to the pure antigorite system. The dehydration temperature of antigorite in this system then remains pressure independent in the computed range of 3–5 GPa.

The composition of the released fluid in the carbonate-bearing systems is a function of both, pressure and temperature. At low pressure and high temperature, significant decarbonation gives rise to an $X(CO_2)$ of 0.15 in the $CaCO_3$-bearing system and as high as 0.35 in the $MgCO_3$-bearing system (Fig. 5b, c). At the experimental pressure range (≥ 2.5 GPa), however, the fluid is essentially pure $H_2O$ and the carbonates remain stable over the whole temperature range.

Figure 6 compares the calculated mineral modes at 2.5 GPa (white line in Fig. 5d–f) of the pure serpentinite and the carbonated serpentinites with the experimental results. As shown by the calculation as well as our experiments, the dehydration of antigorite in the presence of $CaCO_3$

**Fig. 5** Perple_X pseudosection calculations. **a** Pure antigorite-serpentinite. The colour of each stability field reflects the degree of freedom, with brighter colours corresponding to higher degrees of freedom. **b** Antigorite-serpentinite with 20 wt. % of $CaCO_3$. Colour code shows the $X(CO_2)$ of the fluid. Numbered fields contain phase assemblages 1: Atg Chl phA Cpx Mgs Mgt F; 2: Chl Ol phA Cpx Mgs Mgt F; 3: Ol Grt Cpx Mgs Mgt F; 4: Ol Grt Cpx Mgs Arag Mgt F; 5: Chl Ol Cpx Mgs Arag F; 6: Atg Chl Br Mgt Cpx Mgs F; 7: Atg Chl Ol Cpx Dol F; 8: Chl Amph Ol Cpx Dol F; 9: Chl Ol Cpx Dol F; 10: Atg Chl Cpx Arag Mgs Hem F; 11: Atg Chl Br Cpx Mgs Hem F; 12: Atg Chl Mgt Mgs Arag F; 13: Cpx Ol Spl Grt Dol F; 14: Cpx Ol Grt Cal Dol F; 15: Cpx Ol Spl Cal Dol F; 16: Cpx Ol Spl Grt Cal F. **c** Antigorite-serpentinite with 20 wt. % $MgCO_3$, colour coded for fluid $X(CO_2)$. **d–f** The same pseudosection colour coded for the mass fraction of released $H_2O$. Shown are only fields in which dehydration of antigorite occurs. Dashed line corresponds to the isobaric profiles shown in Fig. 6a–c. The coloured arrows mark a warm (orange) and a cold (blue) subduction zone path, taken from Syracuse et al. (2010). The final disappearance of antigorite is highlighted in red.
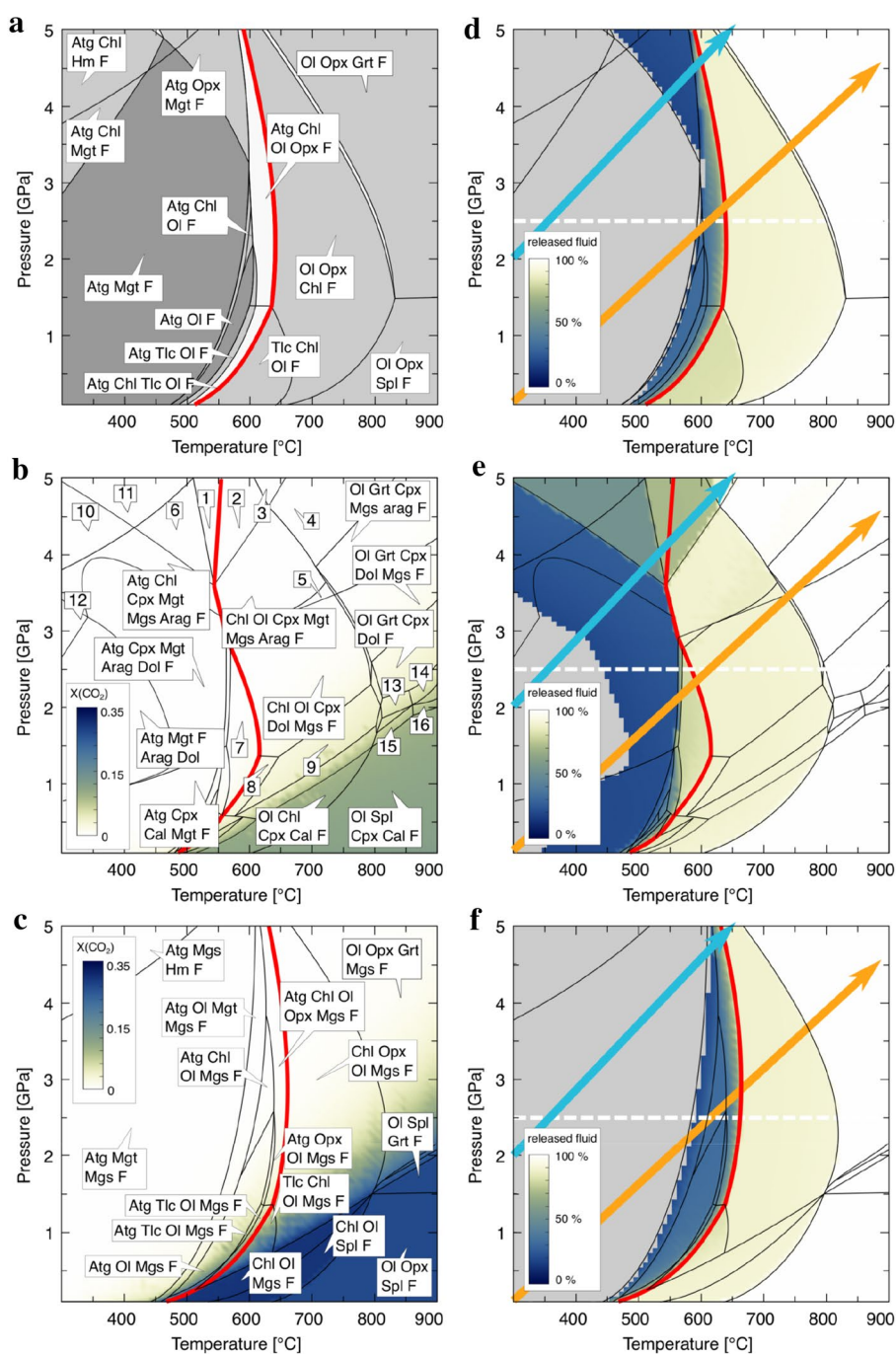


finishes at approximately 580 °C, just over 50 °C lower compared to the carbonate-free system. Over the entire temperature range, however, the experimental total carbonate content remains close to the initial value of 20 wt. %, in agreement with the predicted low $CO_2$ content in the released fluid (compare Fig. 5b) and low solubility of carbonates in aqueous fluids at these conditions (Menzel et al. 2020; Farsang et al. 2021). The experimental results are in very good agreement with the calculations. Major discrepancies are only observed in the relative amount of

olivine and clinopyroxene at elevated temperatures. The system with $MgCO_3$ shows a slightly larger decrease in the total carbonate mode at high temperatures. At the same time, the mode of olivine increases rapidly.

In Fig. 7, we explore the effect of the Ca-carbonate fraction on the antigorite-out reaction in a 3D space. It can be seen that the final dehydration temperature of a pure antigorite, i.e. $CaCO_3$ weight fraction = 0, decreases only slightly with increasing pressure (compare also Fig. 5a). By increasing the $CaCO_3$ content to 20 wt. %, which is similar to our

**Fig. 6** Mineral modes along the outlined isobaric paths at 2.5 GPa ▶ of Fig. 5a–c: **a** Antigorite-serpentinite with 20 wt. % CaCO₃. **b** Pure antigorite-serpentinite. **c** Antigorite-serpentinite with 20 wt. % MgCO₃. Lines are calculated with Perple_X. Points are mass balance results of experiments from this study. Cb refers to total carbonate, i.e. aragonite/calcite + dolomite + magnesite

experiments, a decrease of approximately 50 °C in the antigorite stability is observed in the pressure range 2 GPa–4 GPa, in broad agreement with our experiments. The dehydration temperature at this bulk composition is calculated to decrease further with increasing pressure to about 550 °C at 5 GPa, which is in good agreement with experiment V1153b that contains only 51 wt. % antigorite at 5 GPa and 500 °C. An even more extreme pressure dependence is predicted at a bulk carbonate content of ≥ 25 wt. %. At these compositions, the dehydration takes place at around 580 °C in the range 1 GPa to 3 GPa, but at higher pressures is predicted to decrease drastically to about 300 °C at 5 GPa.

## Discussion

In the following section, we discuss the phase relations in carbonate-bearing serpentinites based on our experiments and thermodynamic calculation. We then use these findings to discuss the release of hydrogen and carbon from subducted carbonated serpentinites. For this discussion, we define the onset of serpentine dehydration, i.e. the onset of fluid release, as the first appearance of secondary phases. The final serpentine disappearance, i.e. antigorite- and lizardite-out reactions, is regarded as the high-temperature boundary of the serpentine dehydration reaction.

### Attainment of equilibrium

The general phase relations and mineral modes observed in our experiments are in good agreement with the thermodynamic calculations (Fig. 6a and b). It is nonetheless important to discuss the state of equilibrium in the experimental products. First, it is important to note that lizardite did not transform to antigorite (Fig. 1b), even at conditions above the expected phase transition (Schwartz et al. 2013), so the lizardite-bearing experiments depict a metastable state. However, since the composition of lizardite and the co-existing phases changes as a function of experimental $PT$-$f(O_2)$ conditions (supplementary material), it can be assumed that the phases are in equilibrium with each other. This is not the case for antigorite, whose $Al_2O_3$ content is 2.5(1) wt. % and does not change as a function of temperature as would be expected from observations in natural serpentinites (Padrón-Navarta et al. 2013; Schwartz et al. 2013). At low temperatures, antigorite
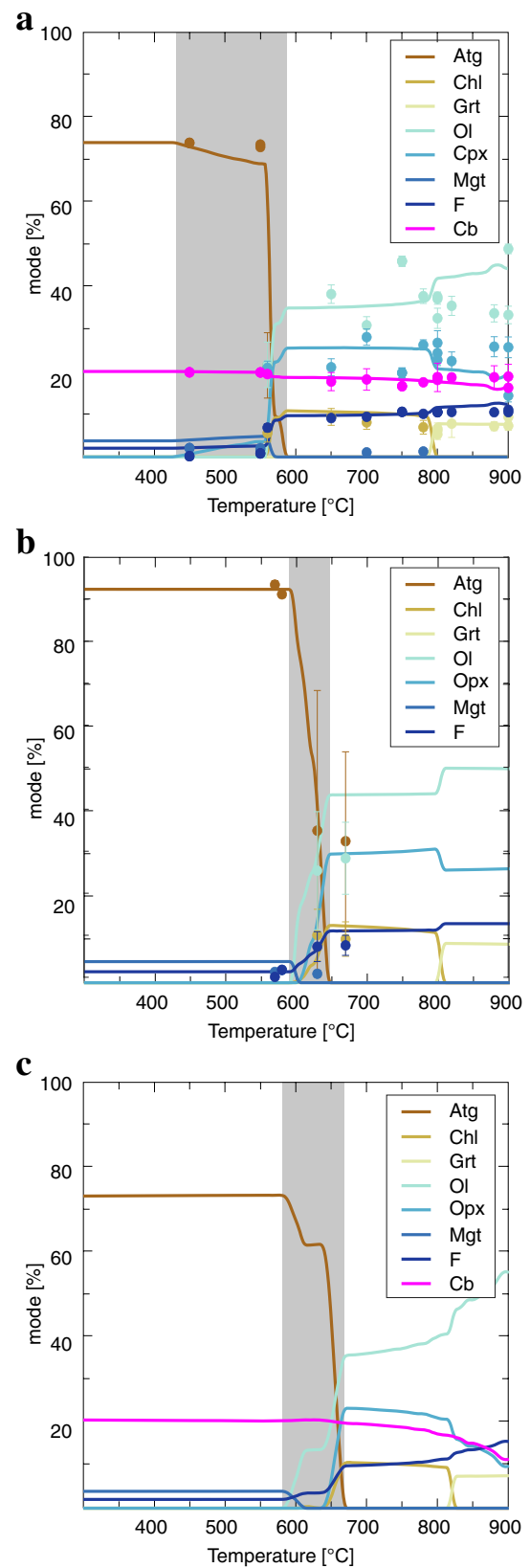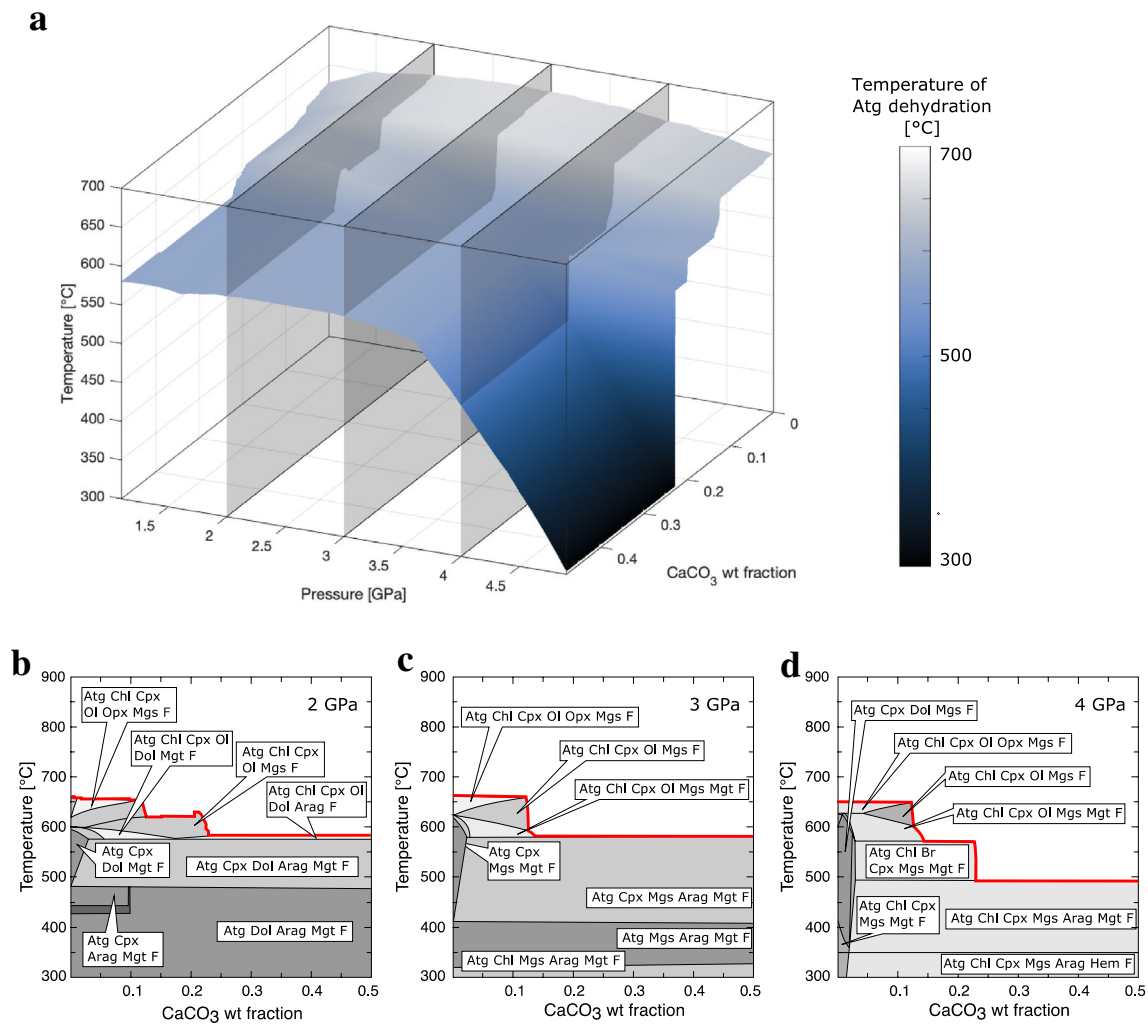
**Fig. 7** The maximum stability of antigorite as a function of P, T and CaCO$_3$ fraction. **a** The antigorite-out surface in the 3D space, colour coded for the maximum temperature at which antigorite is still stable. The three planes show the position of the T-X pseudosections in (**b–d**). **b–c** T-X pseudosections calculated for the pressures 2 GPa, 3 GPa and 4 GPa. The red line represents the maximum temperature at which antigorite is stable
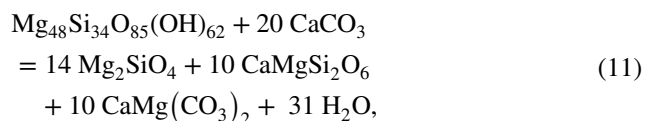
is the sole host of Al and a change in its composition is disabled due to the lack of elemental exchange. However, since even experiments with pronounced dehydration (V1105, V1111, V1234a, V1082) do not show a change in antigorite composition, we assume that this is caused by overall sluggish diffusion kinetics of Al in antigorite. We nonetheless assume that the co-existing phases are in equilibrium with this particular antigorite. The second issue is the formation of diopside in antigorite-bearing experiments at temperature above the expected first appearance of clinopyroxene. Indeed, experiments performed at temperatures ≤ 550 °C do show submicrometric grains along serpentine grain boundaries. Due to this very small grain size, however, we could not unequivocally identify them as reaction products and it might be possible that dehydration

takes place at even lower temperatures than can be determined from experiments.

## Phase relations in a Ca-bearing ophicarbonate system

The onset of dehydration is marked by the appearance of dehydration reaction products. In the antigorite-bearing experiments, clinopyroxene starts to appear at 550 °C (V1234a). From thermodynamic calculations, it might be expected that clinopyroxene is stable already at lower temperatures of 450 °C (Fig. 6a, b). Although lizardite is metastable with respect to antigorite at our experimental conditions (Schwartz et al. 2013), it appears to be much less sluggish when it reacts compared to antigorite. It may,
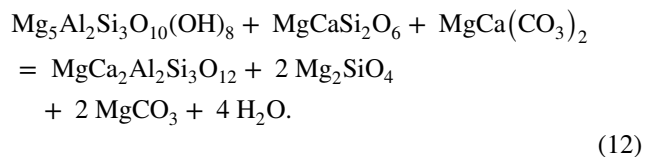
therefore, be a good proxy for antigorite behaviour under equilibrium conditions. In the presence of Ca-carbonate, antigorite starts to breakdown at a temperature at least 100 °C lower compared to the carbonate-free system. This is due to the reaction,
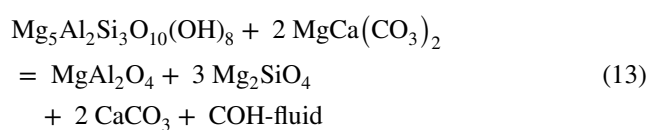
$$
\begin{aligned}
Mg_{48}Si_{34}O_{85}(OH)_{62} + 20\, CaCO_3 \\
= 14\, Mg_2SiO_4 + 10\, CaMgSi_2O_6 \\
+ 10\, CaMg(CO_3)_2 + 31\, H_2O,
\end{aligned}
\tag{11}
$$

which forms dolomite as the main carbonate mineral. Reaction (11) indicates an exchange of Ca and Mg between the carbonate and silicate fractions. The reaction, thus, enables the release of fluids at temperatures $< 500$ °C due to the formation of clinopyroxene. Since carbonate is not consumed in this reaction, this is a simple dehydration reaction in which the $CO_2$ content of the solid fraction is preserved.

Similarly, the maximum temperature to which antigorite is stable is also affected by the presence of $CaCO_3$ and strongly depends on the relative amount of antigorite and $CaCO_3$ in the bulk system (Fig. 7). In the carbonate-free system, antigorite fully dehydrated at 650 °C to olivine, orthopyroxene, chlorite and fluid, with one experiment showing antigorite at temperatures as high as 670 °C. In the presence of $CaCO_3$, only approximately 20 wt. % antigorite remains in the carbonated assemblage by 560 °C implying a reduction in the final antigorite-out temperature of approximately 50 °C compared to the carbonate-free assemblage. Lizardite behaves very similarly to antigorite in the absence of carbonate and completely dehydrates by 650 °C and 3 GPa. However, in the carbonate-bearing experiments, lizardite is almost completely dehydrated at 550 °C and not observed at temperatures $\geq 600$ °C.

The formation of magnesite at higher temperatures and pressures results also from Ca–Mg exchange between the silicate and carbonate fraction. The breakdown of chlorite, for example, favours magnesite formation, which can be described by the reaction,

$$
\begin{aligned}
Mg_5Al_2Si_3O_{10}(OH)_8 + MgCaSi_2O_6 + MgCa(CO_3)_2 \\
= MgCa_2Al_2Si_3O_{12} + 2\, Mg_2SiO_4 \\
+ 2\, MgCO_3 + 4\, H_2O.
\end{aligned}
\tag{12}
$$

The grossular component of garnet is pressure dependent, which favours the formation of magnesite at higher pressures, whereas dolomite forms at pressures $\leq 2.5$ GPa. At even lower pressure conditions ($< 2$ GPa), $CO_2$ is also released to form a COH fluid (Fig. 5b and c). At these conditions, the stable carbonate after chlorite dehydration is calcite and the reaction (12) can be rewritten as

$$
\begin{aligned}
Mg_5Al_2Si_3O_{10}(OH)_8 + 2\, MgCa(CO_3)_2 \\
= MgAl_2O_4 + 3\, Mg_2SiO_4 \\
+ 2\, CaCO_3 + COH\text{-fluid}
\end{aligned}
\tag{13}
$$

This low-pressure reaction causes $X(CO_2)$ values that can exceed 10%, but preserves the Ca-rich nature of carbonates as observed in contact metamorphic environments (Eberhard and Pettke 2021). Such high $CO_2$ contents in combination with an open system fluid flow can cause large-scale carbon release but are only relevant at lower pressures and higher temperatures than experienced in subduction zones (compare Fig. 5).

## Breakdown of serpentine through reaction with graphite

Experiment V1143b where 10 wt. % graphite was added to lizardite at 500 °C and 3 GPa produced an interesting result because lizardite partially broke down to form olivine. In the absence of graphite, lizardite does not start to break down until 550 °C at the same pressure. Magnetite was partially reduced in the experiment causing it to have a porous appearance and resulting in olivine becoming Fe-rich (Mg# = 0.83). It is likely that graphite reduced magnetite. It might be expected that this redox reaction produces carbonates, but they were not found in this experiment. Instead, it would appear that a $CO_2$ gas was produced, which possibly explains the breakdown of lizardite as a result of lowering the $H_2O$ activity through the creation of a COH fluid. This experiment contained Fe–Ir alloy from which the $f(O_2)$ can be calculated from reaction 1 as $-18.5$ log units, i.e. 1.6 log units above FMQ. This value is within the range of the other experiments and certainly at conditions where carbonates should be stable. Importantly, this $f(O_2)$ is above that where carbonates would be in equilibrium with graphite (Fig. 4). As the experiment is graphite saturated, it is possible to estimate the composition of a co-existing COH fluid at these conditions using the method of Holloway (1987) and the equations of state of Belonoshko and Saxena(1991). The result indicates that the fluid would contain 31 mol% $CO_2$ and 69 mol% $H_2O$ with no significant amount of CO, $H_2$ or $CH_4$. This calculation does not consider carbon-bearing complexes, additional solute species as well as the crystallinity of graphite, which are all shown to possibly increase the carbon content of the fluid (Tumiati et al. 2017, 2020; Tiraboschi et al. 2022). The result nonetheless indicates the composition of the fluid, which might explain the partial decomposition of lizardite, which would not start to breakdown until 600 °C in the absence of graphite. It is not clear why a carbonate phase did not form, as previous studies

have shown magnesite to form through the reaction of dilute $CO_2$-bearing aqueous fluids with antigorite at similar conditions (Sieber et al. 2018). Further work would be required to clarify this. Nonetheless, this breakdown reaction at graphite-saturated conditions might be relevant to magnetite-bearing serpentinised rocks that also contain reduced carbon.

## Effect of carbonates on subduction zone phase relations

Ophicarbonates form through hydration and carbonation, of peridotites and comprise essentially serpentinite rocks co-existing with carbonate (Driesner 1993; Kelemen et al. 2011; Schwarzenbach et al. 2013; Clerc et al. 2014; Cannaò et al. 2020). The experiments reported here were designed to examine how such assemblages may respond during subduction, to examine if there are mutual influences on the stability fields of carbon- and hydrogen-bearing phases.

As outlined above, in a Ca-free, $MgCO_3$-bearing system, the dehydration reactions do not change with respect to the pure serpentine along typical subduction zone *PT* gradients (Fig. 5a and c). In a $CaCO_3$-bearing system, on the other hand, the carbonates strongly influence the mineral phase relationships in serpentinites through Ca–Mg exchange between the carbonate and silicate fraction. The dehydration reaction in this system forms the CaMg-silicates clinopyroxene and grossular, whereas the carbonate becomes more Mg-rich as shown in reactions (11) and (12). The calculations indicate that clinopyroxene should start to form at temperature as low as 450 °C at 2.5 GPa. This results in a decrease in the temperature where antigorite starts to dehydrate by approximately 100 °C, compared to the carbonate-free system (Fig. 6a and b). The final dehydration, i.e. the maximum temperature at which antigorite is still observed, additionally depends on the relative amount of Ca-carbonate and antigorite. A system with a bulk Ca-carbonate content of 20 wt. % antigorite fully dehydrated around 50 °C lower in temperature, compared to the carbonate-free system (Fig. 6a and b), which corresponds to about 10 km in depth. In cold subduction zones, where dehydration starts at higher pressures, the decrease in temperature is predicted to reach up to 100 °C. In a system with a higher bulk Ca-carbonate content of ≥ 25 wt. %, the final dehydration temperature is calculated to become strongly pressure dependent (Fig. 7) and in cold subduction zones, antigorite would be fully dehydrated at temperatures of ≤ 500 °C, corresponding to a decrease in temperature of almost 150 °C compared to the carbonate-free system.

Ophicarbonates often form distinct zones within hydrated peridotites (Müntener and Hermann 1996; Pelletier and Müntener 2006). The carbonate content typically varies and can locally reach up to 80 wt. %. Consequently, it can be expected that dehydration takes place in carbonated zones at

conditions where the surrounding hydrated peridotite did not yet undergo dehydration. Whilst the hydrogen is lost through dehydration at lower temperatures, carbonates within ophicarbonate assembles remain stable and are able to transport carbon into deeper levels within subduction zones, in agreement with earlier calculations from Kerrick and Connolly (1998).

In our model, we did not consider carbonate solubilities and dissolved carbon-bearing species other than $CO_2$. The consumption of carbonates in natural samples could, therefore, be higher than our calculation predicts. However, typical *PT* paths of subducted carbonated serpentinites are such, that dissolved $CO_2$ is the main carbon species in the fluid, whereas the overall solubility is expected to be low (Tiraboschi et al. 2022). Carbonated serpentinites can contain high carbonate fractions of > 50% (Driesner 1993; Pozzorini and Früh-green 1996; Eberhard and Pettke 2021) and it is, thus, unlikely that significant carbonate is removed through carbonate dissolution. Furthermore, the change in carbonate composition towards more Mg-rich endmembers with increasing temperature decreases the carbonate solubility by about two orders of magnitude (Farsang et al. 2021), which helps to preserve carbonates to deeper levels in the subduction zone. The extent to which carbonates can be released in subduction zones through dissolution in aqueous fluids will, therefore, strongly depend on the fluid–rock ratio (Menzel et al. 2020). To achieve a significant discharge of dissolved carbonate from the slab towards the mantle wedge requires long-term pulsed or continuous fluid flow (John et al. 2012; Tian et al. 2019).

A subducted slab can also contain reduced carbon (Frezzotti et al. 2011; Galvez et al. 2013; Ague and Nicolescu 2014; Vitale Brovarone et al. 2017; Boutier et al. 2021) and redox reactions with different carbon-bearing phases are plausible. There are a number of equilibria that can be written to describe the $f(O_2)$ at which graphite and carbonates would coexist in the different assemblages encountered in these experiments (reaction (8)–(10)). As shown in Fig. 4, these three equilibria predict $f(O_2)$ values that are within 1 log unit of each other except at the lowest temperature. In comparison to the carbonate-bearing experiments, which did not contain graphite and of which the $f(O_2)$ is mainly dominated by the presence of magnetite, the graphite stability field is at a log $f(O_2)$ approximately 1–2 log units below between 550 °C and 600 °C and approximately 5 log units below by 450 °C. Thus, only quite reduced serpentinites that do not contain magnetite can reach the graphite stability field. Since serpentinisation occurs concurrently with oxidation (Evans 2008), partially to completely serpentinised peridotites are quite oxidised (Debret et al. 2014, 2015; Klein et al. 2014; Iacovino et al. 2020; Mayhew and Ellison 2020) and we expect such extremely reduced serpentinites to be quite rare. Several studies, however, have reported the

formation of graphite through the reduction of carbonates (Galvez et al. 2013; Vitale Brovarone et al. 2017). Vitale Brovarone et al. (2017), for example, found instances of carbonate reduction in ophicarbonates. This is not likely to result from pressure- or temperature-dependent shifts in redox potentials, however, and probably requires infiltration of an external $H_2$-bearing fluid as stated by the authors. A potential $H_2$ source might be the continued hydroxylation of a fresh peridotite reservoir, releasing dry $H_2$, and thereby creating the reducing environment needed for graphite formation (Vitale Brovarone et al. 2020; Boutier et al. 2021). Other studies, however, indicate that serpentinization at high pressure does not cause the release of $H_2$ (Evans 2010).

# Conclusion

In this study, we show that the presence of $CaCO_3$ within serpentinites has a significant effect on the release of water from subduction zones at pressures between 2 and 5 GPa. Serpentine breaks down through a reaction with $CaCO_3$ to form clinopyroxene. This Ca–Mg exchange with the silicate fraction results in a shift of the carbonate towards Mg-rich endmembers. This process causes an early release of an aqueous fluid with a very low $X(CO_2)$, such that the carbonate fraction is preserved. For ophicarbonates containing 20 wt. % $CaCO_3$, the experiments show that serpentine will disappear from the assemblage at a temperature that is approximately 50 °C lower compared to the carbonate-free assemblage at 2.5 GPa. Calculations indicate that the onset of serpentine dehydration may be reduced by up to 100 °C. Further thermodynamic calculations show that the maximum temperature at which antigorite is still stable strongly depends on the relative proportions of $CaCO_3$ and antigorite. For an initial carbonate content of $\geq 25$ wt. %, the antigorite is predicted to be fully dehydrated at temperatures $< 500$ °C in cold subduction zones. Whilst hydrogen is released early through these dehydration reactions, carbon will remain in the rock and can be subducted to great depths unless external fluids cause extensive dissolution of the carbonate minerals. Pseudosection calculations for Ca-free systems containing $MgCO_3$ reveal dehydration temperature ranges similar to the carbonate-free serpentinites.

Graphite-bearing experiments show that graphite is oxidised in the presence of magnetite-bearing serpentinite. The formation of  through the reduction of carbonates would require reducing conditions that are not likely to be reached by typical magnetite-bearing serpentinites. In natural examples where the reduction of carbonates has been found to occur, this most likely required an open system infiltration of $H_2$-rich fluids.

Although the presence of carbonates affects the release of $H_2O$ from serpentinised peridotites in the slab, the $X(CO_2)$ of the fluid remains low, and the extent of aqueous carbonate dissolution is imperceptible in the closed system experiments. Dissolution of carbonates at conditions of serpentine dehydration is likely to be only achieved as a result of a significant external fluid flux.

**Data availability**   All data used in this study can be found in tabulated form in the supplementary material. Colour schemes used in figures are from Crameri (2018).

# Declarations

**Conflict of intrest**   The authors declare that they do have no known competing interests.

# References

Ague JJ, Nicolescu S (2014) Carbon dioxide released from subduction zones by fluid-mediated reactions. Nat Geosci 7:355–360. https://doi.org/10.1038/NGEO2143

Belonoshko A, Saxena SK (1991) A molecular dynamics study of the pressure-volume-temperature properties of supercritical fluids: II. CO2, CH4, CO, O2, and H2. Geochim Cosmochim Acta 55:3191–3208. https://doi.org/10.1016/0016-7037(91)90483-L

Boutier A, Vitale Brovarone A, Martinez I et al (2021) High-pressure serpentinization and abiotic methane formation in metaperidotite from the Appalachian subduction, northern Vermont. Lithos. https://doi.org/10.1016/j.lithos.2021.106190

Bromiley GD, Pawley AR (2003) The stability of antigorite in the system MgO-SiO2-H2O (MSH) and MgO-Al2O3-SiO2-H2O (MASH): The effects of Al3+ substitution on high-pressure stability. Am Miner 88:99–108

Cannaò E, Scambelluri M, Bebout GE et al (2020) Ophicarbonate evolution from seafloor to subduction and implications for deep-Earth C cycling. Chem Geol 546:119626. https://doi.org/10.1016/j.chemgeo.2020.119626

Clerc C, Boulvais P, Lagabrielle Y, de Saint BM (2014) Ophicalcites from the northern Pyrenean belt: A field, petrographic and stable isotope study. Int J Earth Sci 103:141–163. https://doi.org/10.1007/s00531-013-0927-z

Connolly JAD (1995) Phase diagram methods for graphitic rocks and application to the system C-O-H-FeO-TiO2-SiO2. Contrib Miner Petrol 119:94–116. https://doi.org/10.1007/BF00310720

Connolly JAD, Trommsdorff V (1991) Petrogenetic grids for metacarbonate rocks: pressure-temperature phase-diagram projection for mixed-volatile systems. Contrib Miner Petrol 108:93–105. https://doi.org/10.1007/BF00307329

Crameri F (2018) Geodynamic diagnostics, scientific visualisation and StagLab 3.0. Geosci Model Dev 11:2541–2562. https://doi.org/10.5194/gmd-11-2541-2018

Dasgupta R (2013) Ingassing, storage, and outgassing of terrestrial carbon through geologic time. Rev Mineral Geochem 75:183–229. https://doi.org/10.2138/rmg.2013.75.7

Debret B, Andreani M, Muñoz M et al (2014) Evolution of Fe redox state in serpentine during subduction. Earth Planet Sci Lett 400:206–218. https://doi.org/10.1016/j.epsl.2014.05.038

Debret B, Bolfan-Casanova N, Padrón-Navarta JA et al (2015) Redox state of iron during high-pressure serpentinite dehydration. Contrib Miner Petrol 169:1–18. https://doi.org/10.1007/s00410-015-1130-y

Driesner T (1993) Aspects of petrographical, structural and stable isotope geochemical evolution of ophicarbonate breccias from ocean floor to subduction and uplift: an example from Chatillon, Middle Aosta Valley, Italian Alps. Schweiz Mineral Petrogr Mitt 73:69–84

Eberhard L, Pettke T (2021) Antigorite dehydration fluids boost carbonate mobilisation and crustal $CO_2$ outgassing in collisional orogens. Geochim Cosmochim Acta 300:192–214. https://doi.org/10.1016/j.gca.2021.02.030

Evans BW (2008) Control of the products of serpentinization by the $Fe^{2+}$ $Mg_{-1}$ exchange potential of olivine and orthopyroxene. J Petrol 49:1873–1887. https://doi.org/10.1093/petrology/egn050

Evans BW (2010) Lizardite versus antigorite serpentinite: Magnetite, hydrogen, and life(?). Geology 38:879–882. https://doi.org/10.1130/G31158.1

Evans KA, Frost BR (2021) Deserpentinization in subduction zones as a source of oxidation in arcs: a reality check. J Petrol 62:1–32. https://doi.org/10.1093/petrology/egab016

Evans KA, Powell R (2015) The effect of subduction on the sulphur, carbon and redox budget of lithospheric mantle. J Metamorph Geol 33:649–670. https://doi.org/10.1111/jmg.12140

Facq S, Daniel I, Montagnac G et al (2014) In situ Raman study and thermodynamic model of aqueous carbonate speciation in equilibrium with aragonite under subduction zone conditions. Geochim Cosmochim Acta 132:375–390. https://doi.org/10.1016/j.gca.2014.01.030

Farsang S, Louvel M, Zhao C et al (2021) Deep carbon cycle constrained by carbonate solubility. Nat Commun. https://doi.org/10.1038/s41467-021-24533-7

Ferrand TP (2019) Seismicity and mineral destabilizations in the subducting mantle up to 6 GPa, 200 km depth. Lithos 334–335:205–230. https://doi.org/10.1016/j.lithos.2019.03.014

Franzolin E, Schmidt MW, Poli S (2011) Ternary Ca-Fe-Mg carbonates: Subsolidus phase relations at 3.5 GPa and a thermodynamic solid solution model including order/disorder. Contrib Miner Petrol 161:213–227. https://doi.org/10.1007/s00410-010-0527-x

Frezzotti ML, Selverstone J, Sharp ZD, Compagnoni R (2011) Carbonate dissolution during subduction revealed by diamond-bearing rocks from the Alps. Nat Geosci 4:703–706. https://doi.org/10.1038/ngeo1246

Galvez ME, Beyssac O, Martinez I et al (2013) Graphite formation by carbonate reduction during subduction. Nat Geosci 6:473–477. https://doi.org/10.1038/ngeo1827

Guillot S, Hattori KH, de Sigoyer J (2000) Mantle wedge serpentinization and exhumation of eclogites: Insights from eastern Ladakh, northwest Himalaya. Geology 28:199–202. https://doi.org/10.1130/0091-7613(2000)028%3c0199:mwsaeo%3e2.3.co;2

Hermann J, Troitzsch U, Scott D (2016) Experimental subsolidus phase relations in the system CaCO3-CaMg(CO3)2 up to 65 GPa and implications for subducted marbles. Contrib Mineral Petrol 171:84. https://doi.org/10.1007/s00410-016-1296-y

Holland TJB, Powell R (2011) An improved and extended internally consistent thermodynamic dataset for phases of petrological interest, involving a new equation of state for solids. J Metamorph Geol 29:333–383. https://doi.org/10.1111/j.1525-1314.2010.00923.x

Holland T, Baker J, Powell R (1998) Mixing properties and activity-composition relationships of chlorites in the system MgO-FeO-Al2O3-SiO2-H2O. Eur J Mineral 10:395–406. https://doi.org/10.1127/ejm/10/3/0395

Holloway JR (1987) Thermodynamic modeling of geological materials: minerals, fluids and melts. In: reviews in mineralogy. Am Mineral Soc https://doi.org/10.1515/9781501508950

Iacovino K, Guild MR, Till CB (2020) Aqueous fluids are effective oxidizing agents of the mantle in subduction zones. Contrib Miner Petrol 175:36. https://doi.org/10.1007/s00410-020-1673-4

Jabaloy-Sánchez A, Sánchez-Vizcaíno VL, Padrón-Navarta JA et al (2022) Olivine-rich veins in high-pressure serpentinites: a far-field paleo-stress snapshot during subduction. J Struct Geol. https://doi.org/10.1016/j.jsg.2022.104721

Jennings ES, Holland TJB (2015) A simple thermodynamic model for melting of peridotite in the system NCFMASOCr. J Petrol 56:869–892. https://doi.org/10.1093/petrology/egv020

John T, Gussone N, Podladchikov YY et al (2012) Volcanic arcs fed by rapid pulsed fluid flow through subducting slabs. Nat Geosci 5:489–492. https://doi.org/10.1038/ngeo1482

van Keken PE, Hacker BR, Syracuse EM, Abers GA (2011) Subduction factory: 4. Depth dependent flux of H2O from subducting slabs worldwide. J Geophys Res 116:B01401. https://doi.org/10.1029/2010JB007922

Kelemen PB, Manning CE (2015) Reevaluating carbon fluxes in subduction zones, what goes down, mostly comes up. Proc Natl Acad Sci 112:E3997–E4006. https://doi.org/10.1073/pnas.1507889112

Kelemen PB, Matter J, Streit EE et al (2011) Rates and mechanisms of mineral carbonation in peridotite: natural processes and recipes for enhanced, in situ $CO_2$ capture and storage. Annu Rev Earth Planet Sci 39:545–576. https://doi.org/10.1146/annurev-earth-092010-152509

Kelemen PB, Carlos De Obeso J, Leong JA et al (2022) Listvenite formation during mass transfer into the leading edge of the mantle wedge: initial results from oman drilling project hole BT1B. J Geophys Res Solid Earth. https://doi.org/10.1029/2021JB022352

Keppler H, Frost DJ (2005) Introduction to minerals under extreme conditions. Mineral Behav Extreme Cond 6:1–30. https://doi.org/10.1180/emu-notes.7.1

Kerrick DM, Connolly JAD (1998) Subduction of ophicarbonates and recycling of $CO_2$ and H2O. Geology 26:375–378. https://doi.org/10.2475/ajs.281.3.299

Klein F, Bach W, Humphris SE et al (2014) Magnetite in seafloor serpentinite — Some like it hot. Geology 42:135–138. https://doi.org/10.1130/G35068.1

Li XP, Rahn M, Bucher K (2004) Serpentinites of the Zermatt-Saas ophiolite complex and their texture evolution. J Metamorph Geol 22:159–177. https://doi.org/10.1111/j.1525-1314.2004.00503.x

Mayhew LE, Ellison ET (2020) A synthesis and meta-analysis of the Fe chemistry of serpentinites and serpentine minerals. Philos Trans Royal Soc 378:20180420. https://doi.org/10.1098/rsta.2018.0420

Menzel MD, Garrido CJ, López Sánchez-Vizcaíno V (2020) Fluid-mediated carbon release from serpentinite-hosted carbonates during dehydration of antigorite-serpentinite in subduction zones. Earth Planet Sci Lett 531:115964. https://doi.org/10.1016/j.epsl.2019.115964

Müntener O, Hermann J (1996) The Val Malenco lower crust - Upper mantle complex and its field relations (Italian Alps). Schweiz Mineral Petrogr Mitt 76:475–500. https://doi.org/10.5169/seals-57711

Padrón-Navarta JA, Hermann J, Garrido CJ et al (2010) An experimental investigation of antigorite dehydration in natural silica-enriched serpentinite. Contrib Miner Petrol 159:25–42. https://doi.org/10.1007/s00410-009-0414-5

Padrón-Navarta JA, Sánchez-Vizcaíno VL, Hermann J et al (2013) Tschermak's substitution in antigorite and consequences for phase relations and water liberation in high-grade serpentinites. Lithos 178:186–196. https://doi.org/10.1016/j.lithos.2013.02.001

Pelletier L, Müntener O (2006) High-pressure metamorphism of the Lanzo peridotite and its oceanic cover, and some consequences for the Sesia-Lanzo zone (northwestern Italian Alps). Lithos 90:111–130. https://doi.org/10.1016/j.lithos.2006.01.006

Piccoli F, Vitale Brovarone A, Beyssac O et al (2016) Carbonation by fluid-rock interactions at high-pressure conditions: Implications for carbon cycling in subduction zones. Earth Planet Sci Lett 445:146–159. https://doi.org/10.1016/j.epsl.2016.03.045

Piccoli F, Hermann J, Pettke T et al (2019) Subducting serpentinites release reduced, not oxidized, aqueous fluids. Sci Rep 9:19573. https://doi.org/10.1038/s41598-019-55944-8

Pirard C, Hermann J (2015) Focused fluid transfer through the mantle above subduction zones. Geology 43:915–918. https://doi.org/10.1130/G37026.1

Pitzer KS, Sterner SM (1995) Equations of state valid continuously from zero to extreme pressures with H20 and CO2 as examples. Int J Thermophys 16:511–518

Plank T, Manning CE (2019) Subducting carbon. Nature 574:343–352. https://doi.org/10.1038/s41586-019-1643-z

Plümper O, John T, Podladchikov YY et al (2016) Fluid escape from subduction zones controlled by channel-forming reactive porosity. Nat Geosci 10:150–156. https://doi.org/10.1038/ngeo2865

Pozzorini D, Früh-green GL (1996) Stable isotope systematics of the Ventina Ophicarbonate Zone, Bergell contact aureole. Schweiz Mineral Petrogr Mitt 76:549–564

Rüpke LH, Morgan JP, Hort M, Connolly JAD (2004) Serpentine and the subduction zone water cycle. Earth Planet Sci Lett 223:17–34. https://doi.org/10.1016/j.epsl.2004.04.018

Scambelluri M, Bebout GE, Belmonte D et al (2016) Carbonation of subduction-zone serpentinite (high-pressure ophicarbonate; Ligurian Western Alps) and implications for the deep carbon cycling. Earth Planet Sci Lett 441:155–166. https://doi.org/10.1016/j.epsl.2016.02.034

Schwartz S, Guillot S, Reynard B et al (2013) Pressure-temperature estimates of the lizardite/antigorite transition in high pressure serpentinites. Lithos 178:197–210. https://doi.org/10.1016/j.lithos.2012.11.023

Schwarzenbach EM, Früh-Green GL, Bernasconi SM et al (2013) Serpentinization and carbon sequestration: A study of two ancient peridotite-hosted hydrothermal systems. Chem Geol 351:115–133. https://doi.org/10.1016/j.chemgeo.2013.05.016

Sieber MJ, Hermann J, Yaxley GM (2018) An experimental investigation of C-O-H fluid-driven carbonation of serpentinites under forearc conditions. Earth Planet Sci Lett 496:178–188

Stagno V, Frost DJ (2010) Carbon speciation in the asthenosphere: Experimental measurements of the redox conditions at which carbonate-bearing melts coexist with graphite or diamond in peridotite assemblages. Earth Planet Sci Lett 300:72–84. https://doi.org/10.1016/j.epsl.2010.09.038

Sverjensky DA, Stagno V, Huang F (2014) Important role for organic carbon in subduction-zone fluids. Nat Geosci 7:909–913. https://doi.org/10.1038/ngeo2291

Syracuse EM, van Keken PE, Abers GA (2010) The global range of subduction zone thermal models. Phys Earth Planet Inter 183:73–90. https://doi.org/10.1016/j.pepi.2010.02.004

Tian M, Katz RF, Rees Jones DW, May DA (2019) Devolatilization of subducting slabs, part II: volatile fluxes and storage. Geochem Geophys Geosyst 20:6199–6222. https://doi.org/10.1029/2019GC008489

Tiraboschi C, Miozzi F, Tumiati S (2022) Carbon-saturated COH fluids in the upper mantle: a review of high-pressure and high-temperature ex situ experiments. Eur J Mineral 34:59–75

Tumiati S, Tiraboschi C, Sverjensky DA et al (2017) Silicate dissolution boosts the CO2 concentrations in subduction fluids. Nat Commun 8:616. https://doi.org/10.1038/s41467-017-00562-z

Tumiati S, Tiraboschi C, Miozzi F et al (2020) Dissolution susceptibility of glass-like carbon versus crystalline graphite in high-pressure aqueous fluids and implications for the behavior of organic matter in subduction zones. Geochim Cosmochim Acta 273:383–402. https://doi.org/10.1016/j.gca.2020.01.030

Tumiati S, Recchia S, Remusat L et al (2022) Subducted organic matter buffered by marine carbonate rules the carbon isotopic signature of arc emissions. Nat Commun. https://doi.org/10.1038/s41467-022-30421-5

Ulmer P, Trommsdorff V (1995) Serpentine stability to mantle depths and subduction-related magmatism. Science 268:858–861. https://doi.org/10.1126/science.268.5212.858

Vitale Brovarone A, Martinez I, Elmaleh A et al (2017) Massive production of abiotic methane during subduction evidenced in metamorphosed ophicarbonates from the Italian Alps. Nat Commun. https://doi.org/10.1038/ncomms14134

Vitale Brovarone A, Sverjensky DA, Piccoli F et al (2020) Subduction hides high-pressure sources of energy that may feed the deep subsurface biosphere. Nat Commun. https://doi.org/10.1038/s41467-020-17342-x

Wei C, Powell R (2003) Phase relations in high-pressure metapelites in the system KFMASH (K2O-FeO-MgO-Al2O3-SiO2-H2O) with application to natural rocks. Contrib Miner Petrol 145:301–315. https://doi.org/10.1007/s00410-003-0454-1

White RW, Powell R, Phillips GN (2003) A mineral equilibria study of the hydrothermal alteration in mafic greenschist facies rocks at Kalgoorlie, Western Australia. J Metamorph Geol 21:455–468. https://doi.org/10.1046/j.1525-1314.2003.00454.x

Wunder B, Wirth R, Gottschalk M (2001) Antigorite: Pressure and temperature dependence of polysomatism and water content. Eur J Mineral 13:485–495. https://doi.org/10.1127/0935-1221/